Nonequilibrium in normal-conductor/superconductor microconstrictions

A. Hahn and K. Hümpfner
Ruhr-Universität Bochum, Werkstoffe der Elektrotechnik, 44780 Bochum, Germany
(Received 29 June 1994; revised manuscript received 11 October 1994)

By high-current injection from a point contact into bulk superconducting Ta a nonequilibrium state is produced that may be described as a normal bubble within the superconductor half-space. In driving the diameter of this bubble by the external bias we observe two different types of oscillatory behavior of the conductance. At zero magnetic field the quasiparticle current across the droplet is modulated due to geometrical resonances by multiple Andreev and normal reflections. At magnetic fields somewhat below the critical field, the superconducting surrounding of the normal region forms a symmetric dc SQUID. The magnetic flux through the normal region thus modulates a small supercurrent contribution. Equal numerical values of the bubble diameter are obtained by quantitative evaluation of both effects.

I. INTRODUCTION

In previous papers[1,2] we reported nonequilibrium properties of Ag/Ta point contacts under high-current injection conditions. Nonequilibrium was established in a bulk superconductor in this case. While similar phenomena in whiskers, in films, and in several weak-link types has found much attention in the past, there are only few observations on bulk material by other groups. In particular, the quasiparticle interference effects in zero magnetic field reported below have not been observed elsewhere, while there are observations of oscillations in a magnetic field reported by Yanson and co-workers.[3–5] The most interesting aspect of our experimental results was an oscillatory behavior of the conductance vs voltage characteristics, examples of which will be found in subsequent sections. We have attributed these oscillations to geometrical resonances of quasiparticle waves on the N' zone of a $N/c/N'/S$ structure, with N indicating the normal electrode (Ag), c the contact constriction, N' a normal zone in the tantalum half-space with the order parameter being destroyed, and S the remaining superconductor (Ta). Within this interpretation the oscillations were due to a monotonic increase of the width of the N' zone with applied bias, leading to quasiparticle geometrical resonances.

As will be seen, this interpretation is, with minor modifications, basically correct for experiments in zero magnetic field, to which it had first been applied. However, its extension to even more dramatic oscillations in a finite field,[6] although initially looking very promising, subsequently broke down.[7] In fact, despite a large amount of unpublished experimental material we did not succeed in understanding the phenomena until recently, when we became aware of a certain misconception in our formerly given discussion. This misconception consisted in tacitly assuming all of our observed oscillations to have the same physical origin.

In the following, we present evidence that only the oscillations in zero magnetic field are due to quasiparticle resonances. In contrast to this, oscillations observed in a magnetic field are due to a Josephson current contribution, phase modulated by the magnetic flux in a somewhat unexpected topology.

While the foregoing outline was given in order to avoid confusion about previously published results, the plan of this paper is now as follows. Section II contains a short description of sample preparation. In Sec. III we report experimental results concerning the conductance vs voltage characteristics in zero magnetic field. Its nonequilibrium features are discussed in Sec. IV B along the previously given lines. The theoretical basis for this discussion is given in Sec. IV A in terms of a more general $NcS'N'S$ model which reduces to our previous $NcN'S$ model as a special case. The general solution, however, is needed in Sec. VI.

In Sec. V the experimental results in a magnetic field are reported and the questions are outlined following from these results. In Sec. VI we present a proposal concerning the topological and geometrical structure of the nonequilibrium state which is suited to explain both types of oscillations. Moreover, a quantitative test of this proposal is possible giving good support to it. The picture finally arrived at, leads to a rediscussion of the zero-field oscillations in terms of the above-mentioned $NcS'N'S$ model. Finally, Sec. VII contains some concluding remarks.

In the Appendix, an analytical analysis of the generalized model is sketched by solving the Bogoljubov—de Gennes equations[8] and thus deriving the results given without proof in Sec. IV A. A new "multiple-scattering scheme" thereby applied not only simplifies calculations but, moreover, is closely related to the physics of the interference phenomena under question.

II. SAMPLES

The Ta electrode of our contacts is a high-purity single crystal about 2.5 mm in diameter and well sphere shaped on account of its preparation as a melting drop in ultrahigh vacuum. After oxidation in air for about half an hour at room temperature, a 200-nm Ag counterelectrode was evaporated resulting in a tunneling junction with well-developed gap and phonon structures in the electric

characteristics measured at 1.5 K. With the sample still in the helium bath, the tunneling junction was then destroyed by electric shortening applying a bias in the 1-V regime. According to Jansen, Gelder, and Wyder,[9] this procedure is one of two standard ones applied to produce point contacts. As a result, we obtained junctions of 0.2–1.5 Ω resistance with current-voltage characteristics showing the typical features of metallic microconstriction contacts in the normal[9] and, at low bias, in the superconducting state.[10]

For a typical contact resistance of 0.3 Ω, we obtain from the Sharvin formula[11] typically 70 nm for the diameter of the orifice connecting both metals. This is comparable to the low-temperature coherence length of tantalum, $\xi_2=92$ nm,[12] and thus it seems quite natural to expect nonequilibrium effects even at moderate bias.

III. CONDUCTIVITY AT ZERO MAGNETIC FIELD

Figure 1 represents an experimental result at zero magnetic field. The measured differential resistance of a metallic contact is displayed along the negative ordinate axis as a function of applied voltage. Apart from a small nonlinearity, the positive ordinate scale thus represents the differential conductance. A 5% variation in conductance is indicated by the arrows. The figure represents one example of many similar ones obtained for different samples.

At small bias the characteristics approximately follow the standard theory of the *NcS* microconstriction contact as formulated by Blonder, Tinkham, and Klapwijk[10] (BTK), with a Z parameter close to 0.5 in most cases. In Fig. 1, the uppermost curve represents the BTK result for this Z value, the tantalum energy gap value, $\Delta_2=0.72$ meV, and for the actual measuring temperature of 1.40 K. While this theoretical result describes in a satisfactory way the experiment at low energies eU of the quasiparticles injected into the superconductor, say up to about $0.8\,\Delta_2$, marked deviations occur at higher energies. Nevertheless the experimentally observed characteristics are continuous, rather smooth, and reversible up to a hysteretic transition to what may be termed the "high-current branch" of the characteristics. The jumps to the high-current branch and back from it are indicated in Fig. 1 by vertical arrows. These transitions represent themselves even more pronounced in the current than in the conductance characteristics and the reader may recognize this by taking a glance at Fig. 4. Within the high-current branch, the characteristic is smooth and reversible again. Further one may notice that the voltage scale of the high-current branch is roughly an order of magnitude above the gap voltage.

While we are solely interested in the high-current branch in what follows, we here give a few additional comments on observations of the lower-current branch. In fact, deviations from the BTK theory are often much smaller than those represented in Fig. 1. In particular, the extra structure slightly above the gap voltage is often

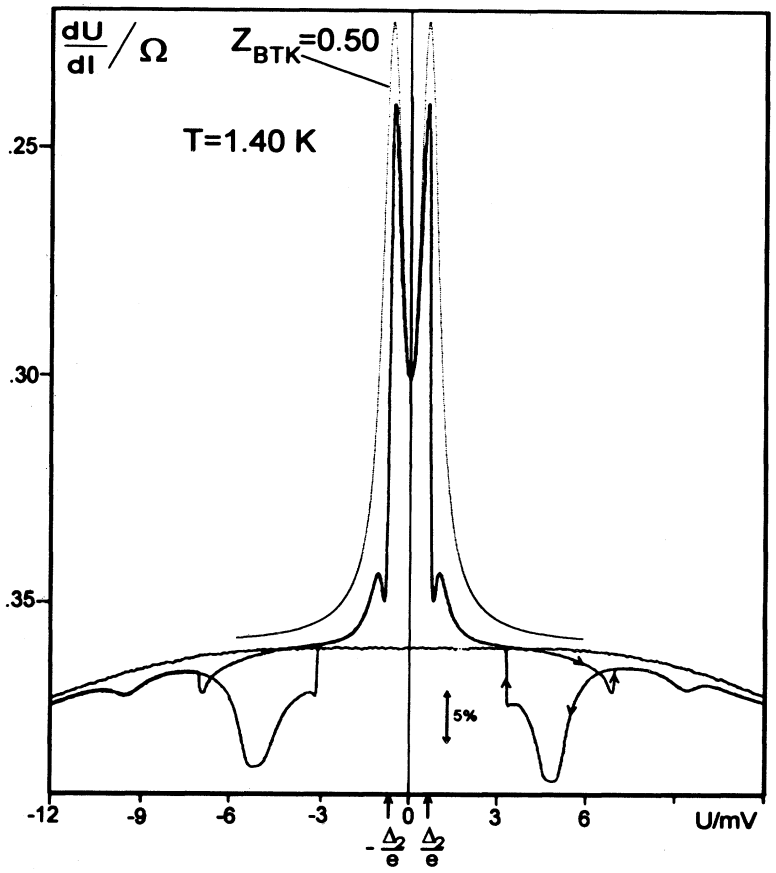

FIG. 1. Differential resistance vs voltage in zero magnetic field for a Ag/Ta microconstriction contact with Ta in the normal and in the superconducting state. BTK theoretical result. High-current branch observable down to 3.5 meV. Gap voltage marked by arrows.

missing, leading to a closer resemblance between theoretical and experimental result not only concerning quantitative but also qualitative aspects. On the other hand, there is no doubt that there is some destruction of the order parameter at low voltage, even within the gap region, as one would expect from the rather large orifice diameters given in Sec. II.

As a main experimental result on the high-current branch of the characteristics we find oscillatory behavior of conductance with up to $3\frac{1}{2}$ periods of oscillation. For the sample represented in Fig. 1 two periods are observed. According to our previously given interpretation these oscillations are due to quasiparticle resonances on an N' zone of destroyed superconductivity below the contact with the width of this zone monotonically increasing with bias. In order to evaluate Fig. 1 numerically, we give a short report on the corresponding one-dimensional (1D) model and of its generalization used in subsequent sections, the generalized results being new.

IV. QUASIPARTICLE RESONANCES

A. Theoretical model

The 1D model is based on the standard BTK treatment[10] of ballistic transport through an *NcS* interface on the basis of the time-independent Bogoljubov–de Gennes equations. Extension of this model to a *NcN'S* structure was given in Ref. 1. Within these models, the bias-dependent normalized excess current is given by

$$I_{\rm exc}(U)=\frac{I_s(U)-I_n(U)}{I_n(\Delta_2/e)}=\int_0^{eU/\Delta_2}\left[\frac{t(\varepsilon)}{t_0}-1\right]d\varepsilon\ , \tag{1}$$

with Δ_2 the gap value in the bulk superconductor (S region), $I_s(U)$ the current with the contact in the superconducting state, $I_n(U)=U/R_n$ the current with the contact in the normal state, at the same bias, $\varepsilon=E/\Delta_2$ the normalized quasiparticle energy,

$$t(\varepsilon)=1+|A(\varepsilon)|^2-|B(\varepsilon)|^2 \tag{2}$$

the current transmission coefficient as defined by BTK, and

$$t_0=t(\infty)=(Z^2+1)^{-1} \tag{3}$$

its value with the contact in the normal state.

The dimensionless parameter Z is the normalized strength of the δ function barrier localized in the constriction (c). $B(\varepsilon)$ and $A(\varepsilon)$ are the energy-dependent reflection amplitudes of the electron and hole waves, respectively, in the N region resulting from an incoming electron entering the contact from the N side.

Let L be the thickness of the N' layer. Then the *NcS* (i.e., BTK) model is a special case ($L=0$) of the *NcN'S* model of Ref. 1. Moreover, we shall need in Sec. VI a more general *NcS'N'S* version of the model taking into account a surface sheet of nonvanishing pair potential on top of the tantalum half-space. With L' the thickness of this surface sheet, and $\Delta_1(\le\Delta_2)$ the value of the pair potential within this sheet, the *NcN'S* model corresponds to the special case $L'=0$.

Direct extension of the previously applied wave-function matching procedure to the *NcS'N'S* case proved difficult leading to rather involved formulas. Therefore a new multiple-scattering scheme was applied to derive results closely related to both the internal structure of the analytical problem and the interference physics. The method is described in the Appendix and the results are given here by Eqs. (4)–(9).

We introduce abbreviations $\alpha_j(j=1,2)$ by

$$\cos\alpha_j=\frac{E}{\Delta_j}=\frac{\Delta_2}{\Delta_j}\varepsilon\ ,$$

$$\text{with } 0<\alpha_j<\frac{\pi}{2} \text{ for } \frac{E}{\Delta_j}<1,\quad i\alpha_j>0 \text{ for } \frac{E}{\Delta_j}>1\ , \tag{4}$$

and the normalized lengths,

$$\lambda=L/\xi',\quad \lambda'=L'/\xi'\ ,$$

$$\text{with } \xi'=(\pi^2/2)\xi_2,\ \text{and } \xi_2=\hbar v_F/(\pi\Delta_2) \tag{5}$$

the tantalum coherence length. Moreover we define a parameter δ by

$$\delta=\frac{i\pi}{2}\frac{\Delta_1}{\Delta_2}\lambda'\sin\alpha_1\ . \tag{6}$$

Then, the final result for $t(\varepsilon)$ may be brought to the form

$$t(\varepsilon)=t_0\frac{[1+|a(\varepsilon)|^2][1-r|a(\varepsilon)|^2]}{|1-r[a(\varepsilon)]^2|^2}\ , \tag{7}$$

with

$$r=1-t_0 \tag{8}$$

the reflection probability of the δ function normal potential barrier and

$$a(\varepsilon)=\frac{\sin\delta-\sin(\delta+\alpha_1)e^{i(\pi\lambda\varepsilon-\alpha_2)}}{\sin(\delta-\alpha_1)-\sin\delta e^{i(\pi\lambda\varepsilon-\alpha_2)}}\quad (NcS'N'S \text{ model})\ , \tag{9}$$

the Andreev reflection amplitude of the tantalum ($S'N'S$) half-space. Obviously, $a(\varepsilon)$ and $t(\varepsilon)$ depend on the model parameters λ, λ', and Δ_1/Δ_2. In particular, the interference effects under question are due to the dependence on λ. This should be kept in mind although for brevity this dependence is not explicitly indicated in the notation with the exception of Eq. (12) below where $t(\varepsilon)$ is replaced by $t(\varepsilon,\lambda)$.

By specializing in two steps to $L'=0$ and $L=0$, respectively, we have

$$a(\varepsilon)=e^{-i\alpha_2}e^{i\pi\lambda\varepsilon},\quad (NcN'S \text{ model}) \tag{10}$$

and

$$a(\varepsilon)=e^{-i\alpha_2}\quad (NcS,\ \text{i.e., BTK model})\ . \tag{11}$$

Inserting (10) or (11) into (7) yields formulas which apart

from notation are equivalent to those given in a less concise form in Refs. 1 and 10, respectively.

Formulas (7) and (9) are new. A sketch of their derivation is given in the Appendix. According to this derivation, (7) holds for any 1D model with a δ-function normal barrier on top of a superconducting half-space $x>0$ regardless of how $\Delta(x)$ varies for $x>0$. $a(\varepsilon)$ has then to be identified with the Andreev reflection amplitude of the S half-space. (7) was used, without derivation, in a previous paper by one of the authors[13] to describe current transmission into a periodic S half-space modeling the layered structure of high-T_c superconductors.

B. Modeling experiments by the *NcN'S* contact scheme

In this subsection we apply the *NcN'S* model to the high-current branch of the characteristics represented in Fig. 1. All necessary formulas were given in Sec. IV A. We do not adjust the Z parameter of the model but instead use its value as taken from the low-current branch of the characteristics, i.e., $Z=0.5$. Since the model parameter Δ_2 has to be identified with the bulk tantalum low-temperature gap 0.72 meV, the only unknown parameter is the thickness of the N' region of destroyed superconductivity, i.e., λ in reduced units. $\lambda(U)$ will be numerically adjusted as a function of bias in the manner to be described below. Before presenting numerical results, we emphasize the following points: Throughout the high-current regime, the voltage U is so far above the gap voltage that contributions to the excess current integral from energies near the upper limit of integration are unimportant, the integrand $t(\varepsilon)/t_0-1$ being very small in this regime. In fact, the oscillations we are interested in are due to contributions from the gap region, ε near unity, to the excess current, and these contributions oscillate with increasing λ. As a consequence, we may replace the upper limit of the integral in (1) by infinity. The result is

$$I_{\rm exc}(U)=\int_0^\infty \left[\frac{t(\varepsilon,\lambda)}{t_0}-1\right]d\varepsilon \ . \tag{12}$$

In contrast with (1), this equation does not only hold for zero temperature but for finite temperature as well. Temperature only enters via the temperature dependence of the model parameter Δ_2 which we neglect throughout. The Fermi distributions of quasiparticle energy in the electrodes do not enter the final result. We refer to Eq. (19) of Ref. 10 which was derived for finite temperature and, apart from notation, coincides with Eq. (12) above.

According to (12), the excess current depends on U only through the U dependence of λ. The oscillations we observe are therefore different in origin from the usual type of Rowell-McMillan oscillations.[14] In the latter case the geometry is fixed and the oscillations occur by variation of energy eU, i.e., variation of the upper limit of the current integral. Roughly speaking, oscillations come about in any case by the phase $\pi\lambda\varepsilon$ in the Andreev reflection coefficient as given in (10). However, while in the Rowell-McMillan case λ is fixed and ε varies, here the most important contributions to the excess current integral come from the vicinity of $\varepsilon=1$, and λ varies with U.

With ε fixed to unity, the current transmission coefficient $t(1,\lambda)$ is periodic in λ with period 1 as may be seen from (7) and (10). This periodicity is also reflected in the excess current (12). Numerical evaluation of the theory now proceeds as follows: On the basis of the formulas of subsection A we could immediately calculate the normalized excess current $I_{\rm exc}(U)$ provided we know how the normalized length λ of the N' zone varies with bias U. In fact we do not.

We may, however, use the model to extract $\lambda(U)$ from the experimental result in the following way: We numerically calculate the excess current as a function of λ. We also calculate its derivative with respect to λ. As a result from numerics, we find the maxima and minima of the derivative,

$$G_\lambda(\lambda)=dI_{\rm exc}(\lambda)/d\lambda \ , \tag{13}$$

rather close to integer and half-integer values of λ, respectively. According to (13) and (1), the normalized differential conductance,

$$G(U)=R_n dI_s/dU \ , \tag{14}$$

is given by

$$G(U)=G_\lambda(\lambda)(\Delta/e)d\lambda/dU+1 \ , \tag{15}$$

and since λ is assumed monotonically to increase with U, the extrema of the experimentally observed conductivity indicate integer and half-integer values of λ. Hence the gross scale of variation of λ along the experimentally determined characteristics is well defined from experiment.

For a more detailed comparison with experiment we assume, for simplicity, λ to increase linearly with voltage U,

$$\lambda=c+dU \ , \tag{16}$$

choosing the parameters c and $d=d\lambda/dU$ such as approximately to reproduce the positions of the maxima and minima of the experimentally determined dI/dU curve. This leads to a scaling of the calculated normalized conductance $G(U)$ according to (15), allowing for a direct comparison with experiment.

There is not too much ambiguity in choosing the parameters c and d except the following: Sometimes there remains some uncertainty in indexing the maxima and minima by integer and half-integer λ values, two possibilities of doing so just differing by unity. An example is given by Fig. 2. Here curve 1 represents the experimentally determined conductance along the high-current branch of Fig. 1 with the ordinate normalized according to (14). More precisely, to account for the slightly non-Ohmic behavior of the normal-state characteristics, the bias-dependent differential resistance $R(U)$ was taken for both the normal and superconducting state from Fig. 1, and the resulting $R_N(U)/R_S(U)$ was plotted as $G(U)$ in Fig. 2, curve 1.

Curves 2 and 3 were calculated with the parameters c and d given in the figure caption and chosen such as to

reproduce the positions on the U scale of the experimentally observed extrema. Somewhat different values of the parameter d resulted from adjusting parameters c and d such as to reproduce the first maximum for 2 but not for 3. As mentioned before, once the abscissa scale adjusted according to (16) the ordinate scale is fixed with no adjustable parameter left.

Not only the U scale is given as an abscissa common to all the experimental and theoretical plots in Fig. 1 but the λ scales for the theoretical curves are displayed as well, illustrating different indexing of the extrema of the experimental characteristics. In discussing the experimental result one may note that λ is measured in units of $\xi'=(\pi^2/2)\xi_2$. In absolute units, ξ' is about five times the coherence length or 0.45 μm.

Curves 4 and 5 will be explained in Sec. VI. Here we restrict discussion to curves 2 and 3. Comparing experimental and theoretical characteristics we do not expect the model to describe the experimental background conductance behavior well within the percentage range of variation under question. However, the oscillation amplitudes should be adequately represented. Apparently, the order of magnitude is roughly accounted for by the theoretical curves, although less satisfactorily by 2 as compared with 3.

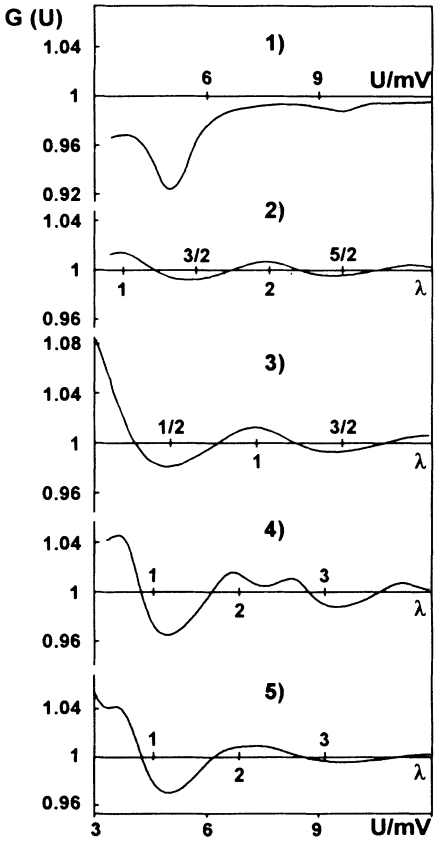

FIG. 2. Normalized conductance $G(U)$ along the high-current branch of Fig. 1. U scale common to all curves, λ scales for theoretical curves. Curve 1: experimental result. Curves 2 and 3: $NcN'S$ model results with parameters $c=0.058$, $d=0.254$ (mV)$^{-1}$ for 2, and $c=-0.587$, $d=0.217$ (mV)$^{-1}$ for 3. Curve 4: $NcS'N'S$ model result with $\Delta_1/\Delta_2=0.5$, $\lambda'=0.2$, $c=-0.974$, $d=0.435$ (mV)$^{-1}$. Curve 5: same as 4 but with $\pm 15\%$ distribution of λ (see text).

In detail, some systematic deviations between experiment and theory are obvious. In the experimental curve, the minima are more pronounced and are narrower on voltage scale as compared with the broad flat maxima. This kind of anharmonicity was observed for all of our samples and is in clear contrast to the theoretical curves. However, the only conclusion to be drawn from this is that λ does not vary linearly with U. Instead, $d\lambda/dU$ must be larger near half-integer than near integer values of λ. This behavior must be looked upon as a hint indicating that quasiparticle constructive or destructive interference is involved in the determination of the bubble diameter at a given bias. Although not just unexpected, this feature must be taken here as a purely experimental result since a theory of $\lambda(U)$ is not available at present. Hence, in order to discuss oscillation amplitudes we neglect this nonlinearity altogether replacing $d\lambda/dU$ by its mean value over, say, two periods.

While curve 3 satisfactorily reproduces the experimental amplitudes, another shortcoming is obvious in this case. The first maximum in the experimental curve is not obtained from curve 3. Taking this maximum serious prevents the indexing of maxima and minima underlying curve 3. Instead, the first maximum must be attributed to $\lambda=1$. As a consequence, we obtain curve 2, which obviously yields too small amplitudes for the low-order oscillations. Now, while there are many reasons for the experimental amplitudes to be smaller than theoretically expected, the reverse situation can hardly be accounted for.

Similar shortcomings are found for other samples and can be found in Ref. 1 on closer examination. Concluding this section we therefore state that although an interpretation of the experiments in terms of quasiparticle resonance phenomena seems possible, in principle, there remain problems to be clarified. Particularly, an independent investigation is highly desired of the main idea presented in the foregoing, namely, the idea of an N'/S phase boundary being driven into the superconductor with its position being experimentally measurable in units of ξ'. Such an investigation is described in the following section.

V. CONDUCTANCE OSCILLATIONS IN MAGNETIC FIELDS

As mentioned before, oscillating contributions to the conductance are observed in the high-current state in magnetic fields somewhat below the critical field. We present two examples in the following figures.

In Fig. 3, the differential resistance is displayed for several values of the external field for the sample the data of which have been displayed in Figs. 1 and 2 for $B=0$. The field was applied parallel to the N/S interface. Because of the demagnetization factor of $\frac{1}{3}$, one has to multiply the denoted external field B_e by 3/2 in order to obtain the true field B at the interface. This holds because

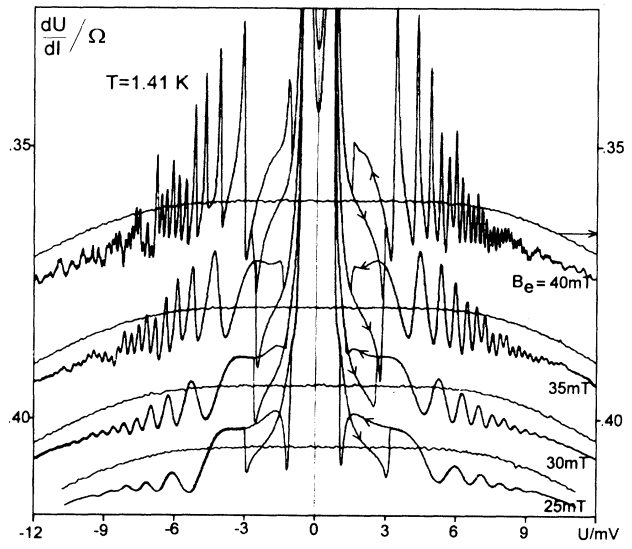

FIG. 3. Differential resistance vs voltage at different values B_e of the external magnetic field. Same sample as in Figs. 1 and 2. The smooth curves correspond to tantalum being brought into the normal state by a high magnetic field of about 400 mT. Curves for different B_e have been displaced vertically, with the ordinate scale corresponding to the uppermost pair of curves. B_e has to be multiplied by $\frac{3}{2}$ to get the true field B at the constriction (see text).

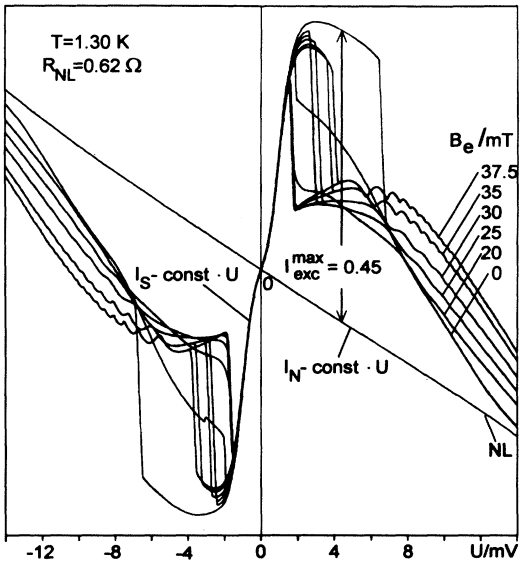

FIG. 4. Current vs voltage characteristics for different magnetic fields. Another contact with properties quite similar to that presented up to now. The same ohmic current contribution, const $\cdot U$, is subtracted from all of the curves including that measured with Ta in the normal state (NL). Thus the difference between any of the curves and that labeled NL equals the bias-dependent excess current. The maximum excess current appears for $B=0$ in the lower current branch of the characteristics. Its value in reduced units (see Sec. IV) is 0.45 as indicated in the figure.

the bulk sphere-shaped tantalum sample is in the Meissner state. The maximum field here thus is $B=60$ mT which corresponds to about 85% of the critical field B_c.

In Fig. 4 the current vs voltage characteristics are shown for another sample. With respect to the normal-state characteristics (NL), the other curves represent the bias-dependent excess current. For a somewhat more detailed description see the figure caption.

Figures 3 and 4 represent two of numerous examples of a new type of oscillatory behavior of characteristics in the high-current state, with up to 50 periods in some cases. These oscillations will be discussed in the following and an explanation will be given. Moreover, there are a number of additional aspects of the experimental results, the most important one being the strong decrease in excess current in the discontinuous and hysteretic transition from the lower- to the high-current state. This behavior is to be analyzed in a current investigation not to be given here. Here we solely are concerned with the oscillations.

As mentioned in the Introduction, these oscillations constituted a puzzle and led to several misinterpretations including the assumption of geometrical resonances of the type described in Sec. IV. Finally, a key towards an adequate understanding was the apparently nonanalytic behavior often observed for the excess current near the oscillation minima. Particularly at the highest fields the minima get more and more cusped indicating a discontinuity in the derivative. Figure 4 may serve as an example. Upon closer examination the phenomenon is also seen in the uppermost curve of Fig. 3. Here the transition from minimum to maximum values of dI/dU is nearly discontinuous. On the whole, the behavior is very much reminiscent of the "Mercereau effect," i.e., the $|\cos(\pi\Phi/\Phi_0)|$ dependence of the maximum current in a symmetric superconducting quantum interferometer containing two weak links with the quantum phase difference between them controlled by an enclosed magnetic flux ϕ. Since the oscillations are best pronounced at fixed external field, see Figs. 3 and 4, flux must be assumed in this case to vary by variation of the area incorporated in the interferometer.

VI. STRUCTURE OF THE NONEQUILIBRIUM STATE

The explanation we finally propose for the observed effects is represented by the highly schematic sketch in Fig. 5, upper part. According to this, the high-current nonequilibrium state implies, in fact, a superconducting quantum interference device (SQUID) topology when discussed in its 3D aspects. In three dimensions, the normal N' region previously introduced must be a normal bubble in the superconductor below the injection orifice. A new idea schematically represented in Fig. 5 is the following: There exists a thin sheet of nonvanishing pair potential immediately below the contact. The structure of the contact in the normal direction is thus given by the order $NcS'N'S$ as depicted in Fig. 5, lower part, instead of $NcN'S$. The thickness of the S' sheet is assumed to be of the order of magnitude of the coherence length, that is rather small compared with the normal bubble diameter.

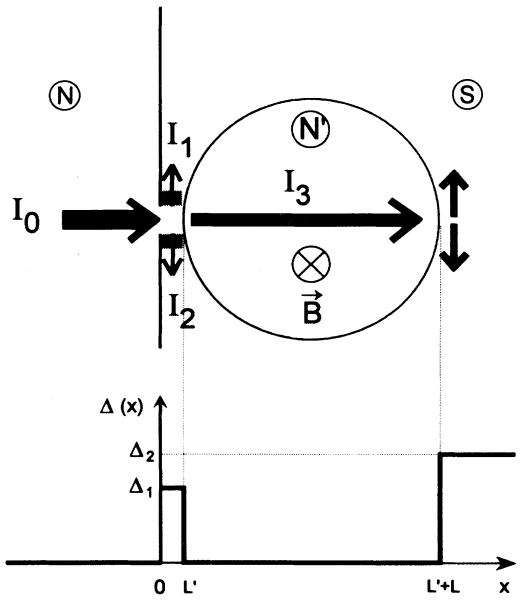

FIG. 5. (Upper part) N, N', and S regions, schematically, indicating topological and geometrical aspects of quasiparticle and supercurrent distribution. I_0, I_3: quasiparticle currents, I_1, I_2: Josephson currents. (Lower part) 1D pair potential model. A quasiparticle injected through the orifice (c) in forward direction meets an $N/c/S'/N'/S$ structure along its path. This model finally leads to the conductance/voltage characteristics displayed as curves 4 and 5 of Fig. 2 (see text).

According to Sec. IV the latter increases along the high-current characteristics from 1 to 3 times ξ', that is from 5 to 15 coherence lengths. A minor fraction of the low-energy injected quasiparticle current is transformed to supercurrent by Andreev reflection within the S' region, while the major rest is transformed to supercurrent deep in the S half-space. This distribution of supercurrents is schematically indicated in Fig. 5. At the end of this section we shall give an argument to explain the existence of the S' sheet. With a magnetic field applied and increased from 0 to near B_c, we expect the topology of the normal bubble to change from that of an imbedded sphere to that of a tube parallel to **B** and intersecting the superconductor surface in some distance.[15] Apparently, this is just the topological situation of a symmetric SQUID. Moreover, the widths of the paths of supercurrents I_1 and I_2 (see Fig. 5) are geometrically restricted near the injection orifice by the dimensions of the orifice itself and by the thickness of the S' sheet. Hence the immediate vicinity of the injection orifice is expected to have weak-link character, the supercurrents I_1 and I_2 being controlled by the pair condensate phase differences across these regions, and these phase differences again controlled by the magnetic flux ϕ through the normal region. As a consequence we expect a maximum Josephson current

$$I_I + I_2 \sim |\cos\pi\phi/\phi_0|, \quad \phi_0 = \frac{h}{2e} , \tag{17}$$

according to the standard textbook formula. In fact this is what we claim to see in the experiments.

If, moreover, we assume that the bubble or tube cross section normal to the field direction does not deviate too much from circular shape, and is nearly B independent, i.e., equal for $B=0$ (spherical bubble) and for $B \approx B_c$ (tube-shaped normal zone) then there is a straightforward proof possible of the above given interpretation. While in Sec. IV we determined at $B=0$ the bubble diameter $L/\xi' = \lambda$ in units of $\xi' = (\pi^2/2)\xi_2$, we may for the same bias determine the tube diameter by counting along the characteristics up to this bias the number of oscillations in a field closely below B_c. We thus obtain the number of flux quanta, ϕ/ϕ_0, at this bias as an experimentally determined quantity. B has to be taken close to B_c because only near $B=B_c$ the field through the normal region is expected to be approximately homogeneous and to take its full value, whereas for $B<B_c$ the field is at least partially expelled on account of the Meissner effect.[15] Setting

$$\frac{\pi}{4} L_B^2 B/\phi_0 = \phi/\phi_0 , \tag{18}$$

we get the magnetically determined bubble diameter L_B and the same quantity in reduced units

$$\lambda_B = L_B/\xi' , \tag{19}$$

which should approximately coincide with the quantity λ obtained from quasiparticle resonances at $B=0$.

The correlation between λ and λ_B is displayed in Fig. 6 for a total of 12 samples, in fact, all those for which experimental data were available. The λ values chosen correspond to maxima and minima in the $B=0$ conductance. The λ_B values were taken for the same bias values at maximum field below B_c. Correlation along the line

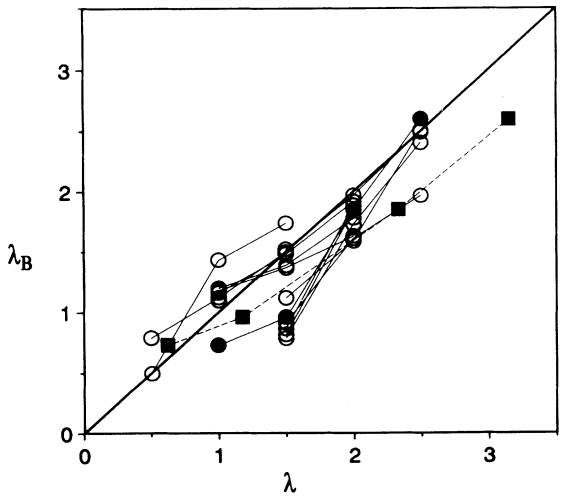

FIG. 6. Linear dimensions of the N' zone: λ from quasiparticle wave resonances at $B=0$, λ_B from counting the number of flux quanta at B closely below B_c. Circles: λ evaluated within the $NcN'S$ model; filled circles: sample of Figs. 1, 2, and 3; filled squares: same sample but λ evaluated within the $NcS'N'S$ model (see text). Connected points correspond to the same sample.

$\lambda=\lambda_B$ could not have been expected to be better in view of the underlying assumptions. Hence we have got a second independent confirmation of the N' zone spatial extent, which we obtained in Sec. IV from the $B=0$ interference phenomena.

Reviewing the preceding discussion it becomes clear that the $NcN'S$ model of Sec. IV may be looked upon as an approximation in the case of very small thickness L' of the S' sheet in Fig. 5. In the one-dimensional model it is, however, not difficult to incorporate this sheet. Assuming some reduction of the pair potential, say, to $\Delta_1<\Delta_2$ and, for simplicity, abrupt transitions in $\Delta(x)$, we obtain the $NcS'N'S$ model given by the lower graph in Fig. 5. The Andreev reflection amplitude $a(\varepsilon)$ from the half-space $x>0$ was given already by formula (9). Assuming fixed values of the parameters Δ_1/Δ_2 and $\lambda'=L'/\xi$, we may numerically calculate the normalized excess current as a function of $\lambda=L/\xi'$ in the manner previously applied for the $NcN'S$ model. Again assuming λ to increase linearly with bias U according to (16), we calculate the normalized differential conductance analogously to Sec. IV B. Curve 4 of Fig. 2 gives the numerical result for the parameters λ', Δ_1/Δ_2, c, and d given in the figure caption.

As expected, this result is richer in structure and less regular than that given by curves 2 or 3, see for example the shallow extra minimum. Such extra structure including flat shoulders not expected from the simpler ($\lambda'=0$) model are often observed for other samples not displayed here. Curve 5 is to show that the shallow minimum does not survive the assumption of a distribution of λ values. Such a distribution must be assumed if one takes into account a spatial distribution of quasiparticle injection directions, i.e., deviations from normal direction. Curve 5 was calculated under the assumption of a rectangular distribution of λ values by $\pm 15\%$. More precisely, in (15) $G_\lambda(\lambda)$ was replaced by the mean value $(1/0.3)\int_{0.85\lambda}^{1.15\lambda} G_\mu(\mu)d\mu$. While a more detailed analysis of experiments in terms of the $NcS'N'S$ model was not yet performed, the example given here shows that under reasonable assumptions concerning the parameters λ' and Δ_1/Δ_2 the modeling of experimental curves is clearly improved.

Finally, the diagram in Fig. 6 has to be slightly modified. For the sample represented in Figs. 1, 2, and 3, and by the filled circles in Fig. 5 we get in the extended model new λ values for the maxima and minima of the dI/dU characteristics. As may be seen from Fig. 2, curves 4 and 5, these values are no longer integer and half-integer. The modified λ vs λ_B correlation is represented by the squares in Fig. 6 with the result that altogether the correlation is neither better nor worse than in the simpler $NcN'S$ model.

After having obtained this interpretation scheme we argue that its main assumption is reasonable. This assumption postulates immediately below the contact a finite S' sheet separating the normal bubble from the surface and hence allowing for a Josephson current in a doubly connected topology. However, such a situation is just what must be expected if the breakdown of pair potential is mainly due to exceeding a critical supercurrent and not to a thermal effect.[16] Immediately below the contact, namely, all injected current is quasiparticle current. The supercurrent is generated by Andreev reflection of quasiparticles from the energy range $E<\Delta_2$ in a finite depth of order of magnitude given by the coherence length. Hence the assumption is quite plausible of a critical supercurrent not immediately below the contact but in some finite depth.

Nevertheless, Fig. 5 should not be taken too literally. It might well be appreciably modified by a microscopic description of Josephson and quasiparticle current distributions but we expect the main idea to remain unaffected, namely, that we are able to measure the cross section of the nonequilibrium region by counting flux quanta at $B\approx B_c$ along the conductance vs voltage characteristics.

VII. CONCLUDING REMARKS

In the foregoing, discussion was restricted to two experimental results concerning geometrical dimensions of a nonequilibrium structure which was termed a "normal bubble" below the superconductor surface. While the quasiparticle resonances at $B=0$ allowed for the determination of a linear dimension of this bubble, λ in reduced units, a Josephson current contribution periodically modulated by the magnetic flux allowed for determining its cross sectional area. Assuming the cross section not to deviate too much from circular shape both results are found to agree. The bubble diameter is thus experimentally measured and, along the experimental characteristics, is found to increase up to about $\lambda=3$ corresponding to $L=1.4\ \mu$m in absolute units.

In spite of this clear result an adequate description cannot be given at present of what may be termed the "internal structure" of the bubble. Any improved description of this structure would have to incorporate the space-dependent phase of the complex pair potential and the corresponding Josephson current densities with pair breaking being expected above some critical value of the external current. The experimentally observed high-current state would then correspond to this pair-breaking regime. A corresponding approach from theory would be highly desirable but lies beyond the scope of this investigation.

ACKNOWLEDGMENT

This work was supported by the Deutsche Forschungsgemeinschaft.

APPENDIX

Results for the $NcS'N'S$ scattering model were given in Sec. IV A. Rather than giving formal derivations we here report on the structure of the analysis leading to these results omitting all details.[17] The model and its analysis are illustrated by Fig. 7, the subdiagrams (a_1)–(f_2) of which will be referred to in what follows without repeating the figure number.

With the interface between the two metals normal to the x axis and localized at $x=0$, subfigures (a_1) and (e_1) represent the pair and normal potentials entering the

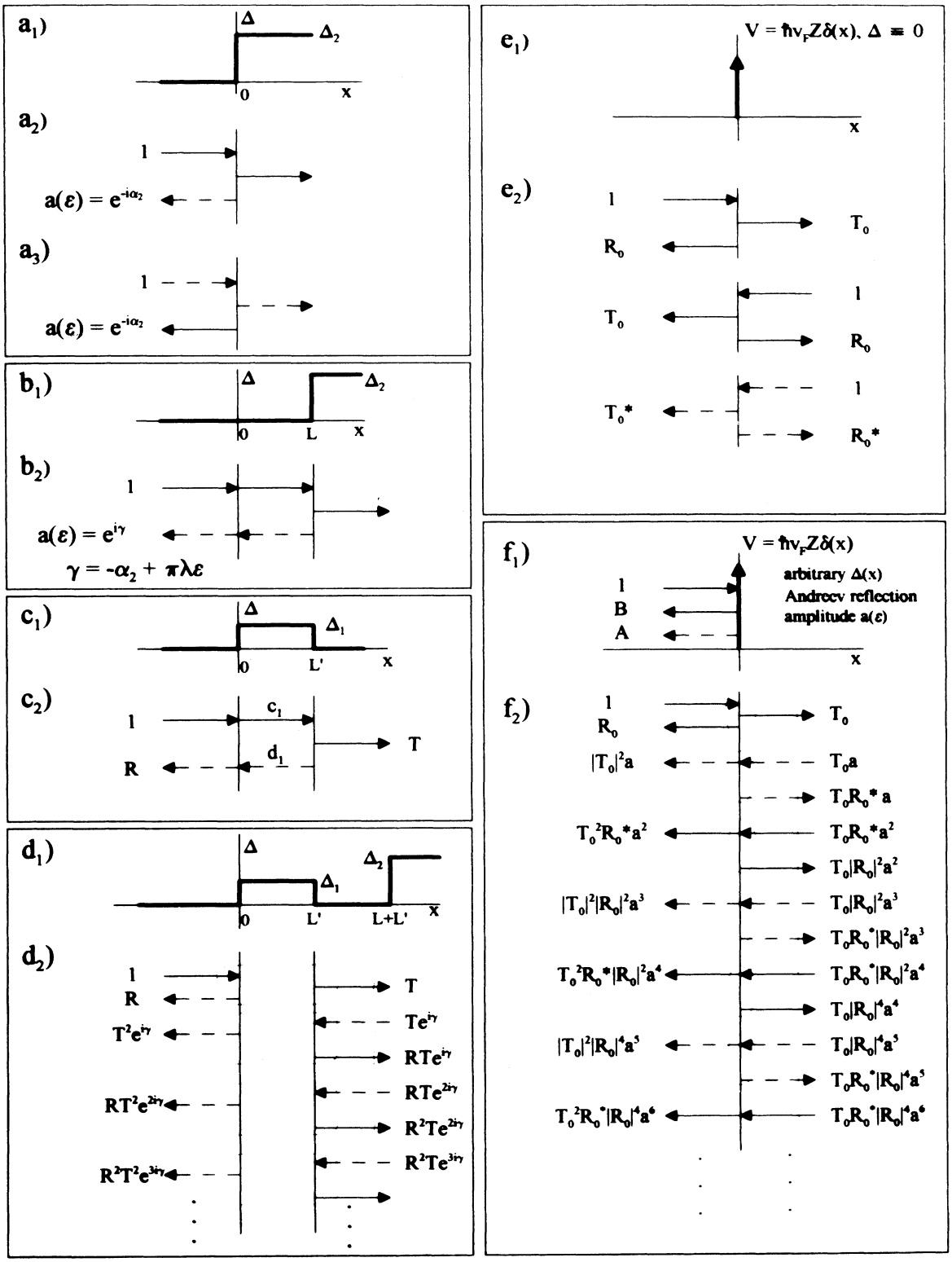

FIG. 7. (a)–(d): Andreev scattering by different pair potentials. Incoming quasiparticle amplitudes normalized to unity. Scattered quasiparticle amplitudes indicated in the figure. In intervals where $\Delta=0$, full arrows indicate electron, dashed arrows indicate hole excitations with the arrow direction indicating the group velocity. The multiple-scattering process in (d_2) is summed up in the text. (e) Normal scattering by a δ-function barrier. (f) combined normal and Andreev scattering. The amplitudes $B(\varepsilon)$ and $A(\varepsilon)$ for normal and Andreev reflection are obtained from the multiple-scattering process (f2) by summing the outgoing electron and hole amplitudes, respectively (see text).

Bogoljubov–de Gennes equations in the *NcS* model of Ref. 10 (BTK). Replacing (a_1) by (b_1) or (d_1) yields the *NcN'S* model of Ref. 1 or, finally, the *NcS'N'S* model under question.

Solving the 1D scattering problem means to determine the electron and hole reflection amplitudes $B(\varepsilon)$ and $A(\varepsilon)$ in the N region as introduced in Sec. IV A. This is done by solving the time-independent Bogoljubov–de Gennes equations for the two-component wave function $\psi(x)$ suitably composed of plane-wave contributions in the different intervals of constant potentials V and Δ. The plane-wave amplitudes in all of the intervals [including the amplitudes $B(\varepsilon)$ and $A(\varepsilon)$ in the N regime] are uniquely determined by the matching conditions at the potential discontinuities and the boundary conditions at $x=\pm\infty$. One obtains an inhomogeneous linear algebraic (4×4) or (8×8) or (12×12) equation system for the *NcS* or *NcN'S* or *NcS'N'S* model, respectively.

Now in the latter case, instead of directly solving the (12×12) system in a rather tedious way, we make use of the internal structure of the problem by composing the final solution from the solutions of more elementary scattering problems. In doing so we obtain the solution in a well-structured analytical form. Moreover the final formulas are more directly related to the physics in terms of a multiple-scattering scheme with constructive and destructive interference of quasiparticle waves determining the final result in a very transparent way.

1. Andreev scattering

First of all, consider the special case $Z=0$, or, equivalently, $V(x)\equiv 0$. Then, as usual, neglecting in the matching conditions small terms of order $(k_F\xi_2)^{-1}$, one obtains pure Andreev scattering or, in terms of Ref. 10, "no scattering across the Fermi surface." That means that for the incoming electron problem under question, in any of the x intervals only the plane waves with wave vectors close to $+k_F$ appear in the solution, with the amplitudes of the "near $(-k_F)$" plane waves vanishing. On the other hand, the matching conditions (postulating continuity of ψ and ψ') are pairwise identical for solutions of this type. Thus, both the number of amplitudes to be determined and equations to be satisfied are smaller than in the $Z\neq 0$ case by a factor of two.

For $Z=0$, the incoming electron solutions for the *NcS* and *NcN'S* models are symbolized in an obvious way by figures (a_2) and (b_2), respectively. The scattering solution is composed in any of the x intervals from electronlike and holelike quasiparticle waves symbolized by full and dotted arrows, respectively. The arrow directions indicate group velocities dE/dk along the corresponding branch of the dispersion relation. Remember that an electron and a hole with a wave vector close to $+k_F$ have positive or negative group velocity, respectively. The corresponding amplitudes are also represented in the figures with the amplitude of the incoming electron normalized to unity. The Andreev reflection amplitudes $a(\varepsilon)$ indicated in (a_2) and (b_2) have already been denoted by formulas (10) and (11) of the main text. They are easily obtained from the corresponding formulas of Refs. 10 and 1 (the abbreviation γ introduced in b_2 is also used in what follows).

On account of electron-hole symmetry, any incoming electron-scattering solution implies an incoming hole solution for the same energy with each plane-wave component

$$\begin{pmatrix} u \\ v \end{pmatrix} e^{ik_F x} e^{i\delta k x}$$

in any of the x intervals replaced by

$$\begin{pmatrix} v \\ u \end{pmatrix} e^{-ik_F x} e^{i\delta k x}$$

in the same interval and with the same amplitude. Subfigure (a_3) gives an example. Both incoming electron and incoming hole solutions are finally needed to construct the solution in the $Z\neq 0$ case.

Next, again for $Z=0$, consider the pair potential barrier of height Δ_1 displayed in (c_1) and representing the *NcS'N'* part of the structure with the S half-space replaced by the N' zone extending to $x=\infty$. The corresponding Andreev scattering of an incoming electron constitutes another type of elementary problem finally entering the general solution. We are not only interested in the Andreev backscattering amplitude denoted by R in this case but also in the transmission amplitude T. Explicitly solving the corresponding (4×4) linear equation system we obtain formulas for R and T. These are given here without detailed derivation. We obtain

$$T=\frac{-\sin\alpha_1}{\sin(\delta-\alpha_1)}\ , \tag{A1}$$

$$R=\frac{\sin\delta}{\sin(\delta-\alpha_1)}\ , \tag{A2}$$

with α_1 and δ given in Sec. IV A. Note T and R depend on ε.

Finally, the Andreev backscattering amplitude $a(\varepsilon)$ produced by the pair potential of the subdiagram (d_1) may be constructed as an infinite series. The multiple-scattering series to be summed over is indicated in subdiagram (d_2). The results of the elementary scattering problems above are incorporated in the amplitudes given in (d_2) in an obvious way. In summing the outgoing hole amplitudes we obtain

$$\begin{aligned} a(\varepsilon)&=R+T^2e^{i\gamma}+T^2Re^{2i\gamma}+T^2R^2e^{3i\gamma}+\cdots \\ &=R+\frac{T^2e^{i\gamma}}{1-Re^{i\gamma}}\ . \end{aligned} \tag{A3}$$

Using (A1) and (A2) and performing some elementary transformations yields

$$a(\varepsilon)=\frac{\sin\delta-\sin(\delta+\alpha_1)e^{i\gamma}}{\sin(\delta-\alpha_1)-\sin\delta e^{i\gamma}}\ . \tag{A4}$$

This is just Eq. (9) of the main text which is thereby derived.

2. Normal scattering

Assume $\Delta(x)\equiv 0$ and $V(x)=\hbar v_F Z\delta(x)$. According to standard textbooks, for an electron with wave number $k_F=mv_F/\hbar$, transmission and reflection amplitudes for the δ-function barrier are given by

$$T_0=\frac{1}{1+iZ},\quad R_0=\frac{-iZ}{1+iZ}\ . \tag{A5}$$

This scattering solution is symbolically displayed in (e_2). Again small deviations δk from k_F may be neglected in T_0 and R_0. With other words, we neglect the energy dependence of T_0, R_0 for excitation energies small compared with E_F. As indicated in subdiagram (e_2), the corresponding amplitudes for a hole excitation are T_0^* and R_0^*. (A5) implies the properties

$$|T_0|^2+|R_0|^2=1;\quad T_0R_0^*=-T_0^*R_0\ . \tag{A6}$$

3. Combined normal and Andreev scattering

We are interested in the case of combined normal and Andreev scattering. Without normal scattering, i.e., for $Z=0$, Andreev reflection from the half-space $x>0$ is completely described by the energy-dependent Andreev reflection coefficient $a(\varepsilon)$. For nonvanishing Z, the reflected electron and hole amplitudes, $B(\varepsilon)$ and $A(\varepsilon)$, have to be calculated, which were introduced in context with Eq. (2) of the main text.

Figure 7(f) illustrates the situation. In order to apply a multiple-scattering scheme very similar to that used above we introduce instead of the given $\Delta(x)$, a pair potential which is identical to $\Delta(x)$ everywhere except for $0<x<\delta^+$ where $\Delta(x)$ is set zero. δ^+ is a positive infinitesimal introduced solely to define plane-wave amplitudes in this interval. With $\delta^+\to 0$ the problem is identical to the original one. In subdiagram (f_2) the right-hand plane-wave amplitudes are defined in this infinitely small interval.

The multiple-scattering scheme is now straightforward, all partial wave amplitudes being denoted in the diagram. Summing all of the outgoing electron contributions yields, with $a(\varepsilon)$ replaced by a for brevity,

$$\begin{aligned}B(\varepsilon)&=R_0+T_0^2R_0^*a^2(1+|R_0|^2a^2+|R_0|^4a^4+\cdots)\\&=R_0+\frac{T_0^2R_0^*a^2}{1-|R_0|^2a^2}=\frac{R_0+(T_0^2R_0^*-R_0|R_0|^2)a^2}{1-|R_0|^2a^2}\\&=R_0\frac{1-a^2}{1-|R_0|^2a^2}\ .\end{aligned} \tag{A7}$$

Here use was made of (A6). For the reflected hole amplitude we obtain

$$\begin{aligned}A(\varepsilon)&=|T_0|^2a(1+|R_0|^2a^2+|R_0|^4a^4+\cdots)\\&=\frac{|T_0|^2a}{1-|R_0|^2a^2}\ .\end{aligned} \tag{A8}$$

After some straightforward calculation, not to be given here, we obtain from this the current transmission coefficient in the form

$$\begin{aligned}t(\varepsilon)&=1-|B|^2+|A|^2\\&=|T_0|^2\frac{(1+|a|^2)(1-|R_0|^2|a|^2)}{|1-|R_0|^2a^2|^2}\ .\end{aligned} \tag{A9}$$

With the previously introduced notation $t_0=|T_0|^2$ and $r=|R_0|^2$ for the normal barrier transmission and reflection probabilities, (A9) is identical to formula (7) of the main text which thereby is proven.

[1] A. Hahn, Phys. Rev. B **31**, 2816 (1985).

[2] A. Hahn and H. Lerchner, in *Proceedings of the 17th International Conference on Low Temperature Physics, Karlsruhe, 15-22 August, 1984,* edited by U. Eckern, A. Schmidt, W. Weber, and H. Wühl (North-Holland, Amsterdam, 1984), Pt. II, DL9, p. 803.

[3] I. K. Yanson, L. F. Rybal'chenko, N. L. Bobrov, and V. V. Fisun, Fiz. Nizk. Temp. **12**, 552 (1986) [Sov. J. Low Temp. Phys. **12**, 313 (1986)].

[4] I. K. Yanson, N. L. Bobrov, L. F. Rybal'chenko, and V. V. Fisun, Fiz. Nizk. Temp. **13**, 1123 (1987) [Sov. J. Low Temp. Phys. **13**, 635 (1987)].

[5] I. K. Yanson *et al.*, Fiz. Nizk. Temp. **14**, 1557 (1988) [Sov. J. Low Temp. Phys. **14**, 639 (1988)].

[6] A. Hahn and K. Hümpfner, in *Proceedings of the 18th International Conference on Low Temperature Physics, Kyoto 1987* [Jpn. J. Appl. Phys. **26**, Suppl. 26-3, 1599 (1987)].

[7] A. Hahn and K. Hümpfner (unpublished).

[8] P. G. de Gennes, *Superconductivity of Metals and Alloys* (Benjamin, New York, 1966), Chap. 5.

[9] A. G. M. Jansen, A. P. van Gelder, and P. Wyder, J. Phys. C **13**, 6073 (1980).

[10] G. E. Blonder, M. Tinkham, and T. M. Klapwijk, Phys. Rev. B **25**, 4515 (1982).

[11] Yu. V. Sharvin, Zh. Eksp. Teor. Fiz. **48**, 984 (1965) [Sov. Phys. JETP **21**, 655 (1965)].

[12] J. P. McEvoy, D. P. Jones, and J. G. Park, Phys. Rev. Lett. **22**, 229 (1969). Coherence length and gap parameter of pure bulk Ta are given the index 2 here and in the following in view of the nomenclature used in the Appendix.

[13] A. Hahn, in 1st *International Conference on Point-Contact Spectroscopy, Kharkow 1991;* Fiz. Nizk. Temp. **18**, 631 (1992) [Sov. J. Low Temp. Phys. **18**, 447 (1992)].

[14] J. M. Rowell and W. L. McMillan, Phys. Rev. Lett. **16**, 453 (1966).

[15] Once the existence of the normal zone is presumed, at finite B an intermediate state must develop and have the claimed properties at least at B close to B_c.

[16] Weak temperature dependence of our results independently indicates that thermal heating is not essential. A detailed analysis of this point is being prepared.

[17] A more exhaustive version of the analysis may be obtained from the authors.